Surface Structure of Hydroxylated and Sulfated Zirconia. A Periodic Density-Functional Study[†]

Alexander Hofmann* and Joachim Sauer

Institut für Chemie, Humboldt-Universität zu Berlin, Unter den Linden 6, D-10099 Berlin, Germany

Received: February 20, 2004; In Final Form: April 19, 2004

The surface structure of sulfated zirconia (SZ) is examined by density-functional theory (DFT) with periodic boundary conditions. Adsorption of H_2O and SO_3 (or H_2SO_4) on the (101) surface of tetragonal zirconia is studied for different loadings up to $H_2SO_4 \cdot 3H_2O$ and $2H_2SO_4 \cdot 2H_2O$ per two surface unit cells (four Zr surface sites). The considered surface species include H_2O, $[H^+,OH^-]$, SO_3, $[H^+,HSO_4^-]$, $[2H^+,SO_4^{2-}]$, $[H^+,HS_2O_7^-]$, and $[2H^+,S_2O_7^{2-}]$. Statistical thermodynamics is used to evaluate the relative stability of different surface structures for different temperatures and pressures of H_2O and SO_3 (or H_2SO_4). The simulated surface phase diagrams show a strong dependency on the considered sulfur species (H_2SO_4 or SO_3) as well as on pressure and temperature. Monosulfates and pyrosulfates may occur, but higher condensated sulfates are not observed. In agreement with infrared experiments, we predict transformation of water-rich structures, $[SO_4^{2-},2H^+,3H_2O]$, into pyrosulfate structures, $[S_2O_7^{2-},2H^+,H_2O]$, during calcination. Further increase of the temperature yields adsorbed SO_3 before the clean surface is reached. Water adsorbed on the t-$ZrO_2(101)$ surface leaves in three steps upon heating from 250 to 730 K at 0.01 bar pressure: physisorbed water below room temperature, the first chemisorbed water at about 440 K and the last water at about 730 K.

1. Introduction

Catalytic properties of sulfated zirconia (SZ) have been published first as a U.S. patent in 1962.[1] It was not before 1979 that Arata et al. report the capability of SZ to catalyze *n*-alkane isomerization near room temperature.[2,3] Since then, a large number of investigations have been made, and the potential use of SZ in acid−base catalysis has been intensely discussed. The major advantage of SZ over other isomerization catalyst, e.g. acidic zeolites, is the lower process temperature[4] and the shift of the thermodynamic equilibrium to the products, i.e. to isobutane. Active SZ is based on tetragonal zirconia as the prevailing phase. SZ based on the more stable monoclinic ZrO_2 phase is not completely inactive as long believed, but much less active than tetragonal SZ.[5]

Santiestaban and co-workers[6] studied the surface structure of SZ by high-resolution transmission electron microscopy (HRTEM) and found that the (110) plane of tetragonal zirconia is the most abundant crystallographic plane. The structure of sulfate itself was not resolved. We know from earlier computational work[7] that 2- or 3-fold coordinations of sulfate species are possible and that the preferred one is different for the (101) and (001) surface. Water is almost ubiquitously present at zirconia surfaces. First of all, many syntheses of zirconia catalysts are made in aqueous solution,[2] and handling SZ under normal laboratory environment leads to water adsorption on the surface depending on the temperature and partial pressure of the water. Even at high temperature, e.g. during calcination, zirconia loses only part of its surface hydroxyl groups.[8]

Much effort has been spent to understand the nature of the surface acidity. In the beginning, SZ was thought to be a superacid,[3] but nowadays there seems to be a consensus that

SZ exhibits acidity, but *not* superacidity.[7,9,10] Haw et al. investigated the relationship of Brønsted and Lewis acid sites by magic angle spinning nuclear magnetic resonance (MAS NMR) studies of pyridine and trimethylphosphine adsorption.[9,11] They did not find any connection between the sulfur content and the number of Brønsted sites in the sample. The number of Brønsted centers was only about 7% of the sulfur content. By adding water to these SZ systems more Brønsted sites are created, which is not the case for sulfate-free zirconia. Nevertheless butane isomerization reaction does not take place, if either only Brønsted sites or only Lewis sites are present.[12]

Previous quantum mechanical studies on SZ used both cluster models and periodic slab models. An early study of the adsorption of H_2O and SO_3[13,14] used a cluster model with a single Zr surface atom surrounded by the right number of oxygen atoms around. A later study of the hydration of isobutene on SZ[15,16] adopts a model with a nonrealistic tetrahedral coordination of Zr.

Pisani and co-workers[17] investigated the adsorption of water on different ZrO_2 surfaces. They applied periodic boundary conditions but were not able to optimize the structures at this time. Haase and Sauer[7] applied periodic boundary conditions in their density-functional theory (DFT) study of the surface structure of SZ. The study was limited to loadings of up to one SO_3 and one H_2O molecule per four Zr surface sites. They showed that different coordinations of SO_3 are stable on different surfaces. Comparison with H-ZSM5 revealed that SZ is not a strong Brønsted acid. The simulated IR frequencies explain observed changes of IR spectra on calcination. Kanougi and co-workers[18] found a new SO_3 adsorption structure, in which one oxygen atom moves out of the zirconia surface and generates a sulfate-like species. They used in their study a two-layer periodic slab model, in which no zirconium atom has a bulklike coordination. Finally, Galvan et al.[19] stressed the modification of the electrostatic potential by H_2SO_4 or H_2O on

Hydroxylated and Sulfated Zirconia Surfaces

J. Phys. Chem. B, Vol. 108, No. 38, 2004 **14653**

the pure tetragonal zirconia (110) surface. They concluded that the strong electrostatic potential in the vicinity of a sulfate group influences the orbital energies of the methane molecule in such a way that they might be more easily accessible for a methane−surface interaction. The effect strongly depends on the degree of dissociation of H_2SO_4 and cannot be achieved by surface hydroxylation.

The aim of this study is to investigate possible adsorption structures of H_2O and SO_3 or H_2SO_4 in different combinations and for different coverages on the t-ZrO_2(101) surface. Compared to the study of Haase and Sauer,[7] we consider higher loadings of H_2O and SO_3. To find out which structures may be the most stable under given conditions (temperature and partial pressure of H_2O, SO_3, and H_2SO_4), we apply molecular statistics and construct surface phase diagrams.

2. Methods

2.1. Computational Details. DFT[20,21] calculations with periodic boundary conditions are carried out with the program package VASP 4.4.5[22−24] using the message passing implementation on a Hitachi SR-8000 F-1 and an IBM p690 turbo. We use the gradient-corrected Perdew−Wang functional PW91.[25−27] Core electrons are described within the projector augmented wave scheme,[28] improved and adapted into VASP by Kresse and Joubert.[29] We use an [Ar] $3d^{10}$ core for Zr, while the $4s^2 4p^6 5s^2 4d^2$ electrons are treated explicitly. Only the electrons in the valence shell are explicitly considered for S and O. The 1s orbital of hydrogen is treated as a valence orbital. The valence electrons are described by a plane wave basis set with an energy cutoff of 400 eV. Geometry optimizations are carried out with a conjugate-gradient algorithm as implemented in the program until convergence of 1 meV of the total energy is reached.

The tetragonal zirconia bulk structure is optimized, starting from the experimental structure with a $4 \times 4 \times 4$ Monkhorst−Pack k-point mesh[30] for the Brillouin-zone sampling and a plane wave cutoff of 800 eV. The deviation of the simulated parameters from the experimental one is smaller than 1% ($a = 3.64_2$ Å, $c = 5.29_4$ Å vs $a = 3.64$ Å, $c = 5.27$ Å (exp)[31]). The strain on the t-ZrO_2 unit cell is also converged to a reasonably small value at this energy cutoff (|strain| < 1 kbar). We minimize the Pulay stress arising from the incomplete basis set by restarting the optimization until self-consistency of the total energy is reached. It is necessary for bulk optimizations to increase the cutoff as far as possible (800 eV) in order to minimize Pulay stress.[32] For slab calculations with fixed lattice parameters where only fractional coordinates are varied, we go back to an energy cutoff of 400 eV. This procedure has neither a significant influence on the optimized structures nor on the calculated adsorption energies. Total energies of selected systems are listed in Table S1 of the Supporting Information.

A 1×2 surface cell of the t-ZrO_2(101) is used in all adsorption simulations. It includes four Zr surface atoms which miss one coordination compared to the bulk. We have shown[7,33] that a five-layer slab is sufficient to get converged surface energies. In the present model, we fix the positions of the atoms in the three bottom layers to their (optimized) bulk positions and calculate the adsorption on the topmost layer. The lattice parameter c was set to 30 Å. This relates to a vacuum size of approximately 15 Å, which is large enough to avoid surface−surface interactions. The cell parameters of our surface slab model are therefore $a = 6.425$ Å, $b = 7.284$ Å, and $c = 30.000$ Å. Convergence of the Monkhorst−Pack k-point mesh has been carefully checked for the H_2O adsorption energy. With a 2×2

$\times 1$ mesh (two different k-points) the deviation from a better k-point mesh is smaller than 1 kJ/mol (better than 1%). The Gibbs free energies are calculated with the harmonic oscillator−rigid rotator−ideal gas approximation. Additionally, the molecules are not allowed to react with each other in the gas phase. The calculation of the frequencies and chemical potentials of the molecules is carried out with Gaussian98.[34] The PW91 functional and Dunning's correlation consistent basis sets (cc-pVQZ) are employed.[35]

2.2. Thermodynamics. For comparison of different compositions of the adsorbates, we consider the formation reaction

$$ZrO_2(101) + nSO_3 + mH_2O \rightleftharpoons [ZrO_2(101), nSO_3, mH_2O] \quad (1)$$
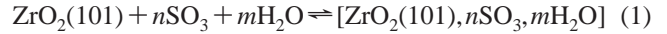
The related Gibbs free energy of adsorption is

$$\Delta G_a = \Delta G_a(T, p_{SO_3}, p_{H_2O}) \quad (2)$$

$$= G^{(s)}_{[ZrO_2(101), nSO_3, mH_2O]} - G^{(s)}_{ZrO_2(101)} -$$
$$n\mu^{(g)}_{SO_3} - m\mu^{(g)}_{H_2O}$$

The Gibbs free energies of the solid and the chemical potential of the gas-phase species are as follows:

$$G^{(s)} = E_0 - RT \ln Q_{vib} \quad (3a)$$

$$\mu^{(g)} = \mu^{(g)}(T, p) = E_0 - RT \ln(Q_{vib} + Q_{rot} + Q_{trans}) + RT \quad (3b)$$

where

$$E_0 = E_{el} + E_{ZPV} \quad (4)$$

Volume changes of solid components are neglected and the volume work of the gas phase is replaced by RT (ideal gas). E_0 is the total (electronic) energy as obtained by DFT plus the zero-point vibrational energy, E_{ZPV}. Q_x are the partition functions for vibrations, rotations, or translations.

It is convenient to reference the chemical potentials of the gas-phase species to the chemical potential at 0 K as a standard. At 0 K the chemical potential is identical to the energy, E_0:

$$\mu^{(g)}(0 \text{ K}) = E_0 \quad (5)$$

The chemical potential relative to this standard, $\Delta\mu^{(g)}$, is

$$\Delta\mu^{(g)} = \mu^{(g)} - E_0 = -RT \ln(Q_{vib} + Q_{rot} + Q_{trans}) + RT \quad (6)$$

For solids, calculation of vibrational frequencies is much more demanding than getting the total (electronic) energy. Vibrations do not contribute to the pressure dependence of the chemical potentials for the gas-phase species. Therefore vibrational contributions are sometimes only roughly estimated or neglected.[36] We will consider neglect of vibrational contributions as an additional approximation:

$$G^{(s)} = E_{el} \quad (7a)$$

$$\mu^{(g)} = E_{el} - RT \ln(Q_{rot} + Q_{trans}) + RT \quad (7b)$$

$$\Delta\mu^{(g)} = -RT \ln(Q_{rot} + Q_{trans}) + RT \quad (8)$$

We finally get

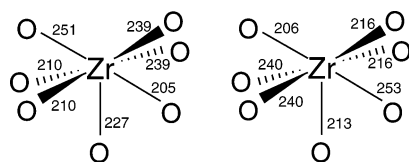$$\Delta G_a = \Delta E_a - n\Delta\mu_{SO_3} - m\Delta\mu_{H_2O} \quad (9)$$

Figure 1. The two different metal sites at the t-ZrO₂(101) surface. The left zirconium atom loses a strong Zr—O bond; the right loses a weak Zr—O bond. The sites are marked as Zr(s) and Zr(w), respectively. The bulk bond lengths are 210 and 243 pm for strong and weak Zr—O bonds, respectively.

with

$$\Delta E_a = E_{\text{adsorbate}} - E_{\text{pure}} - nE_{SO_3} - mE_{H_2O} \qquad (10)$$

where E is either E_0 or E_{el}, depending on the level of approximation. Equation 9 shows that adsorption is only observed ($\Delta G_a < 0$) if the adsorption energy is negative enough to overcome the entropy loss of the translating and rotating gas-phase molecules when they bind to the surface.

3. Results

3.1. Water Adsorption. Two different types of Zr—O bonds are found in bulk t-ZrO₂ (Figure 1). Each Zr atom forms four strong Zr—O bonds with a bond length of 2.10 Å and four weak bonds with bond lengths of 2.43 Å (calculated values). This results in two different types of Zr surface sites on a t-ZrO₂-(101) surface.[7] One misses a short, strong Zr—O bond, Zr(s); the other, a long, weak Zr—O bond, Zr(w). Adsorption is expected to be stronger at the (s)-site with the missing short bond and weaker at the (w)-site with the missing long bond. The t-ZrO₂(101) 1 × 2 surface slab contains two of each of these zirconium sites. Haase and Sauer[7] examine the adsorption of a single water molecule and find molecular adsorption on the weak sites, but dissociative adsorption on the strong sites with adsorption energies of −105 and −194 kJ/mol, respectively. In contrast, in this study a single water molecule dissociates also on the (w)-site. A terminal and a bridging hydroxyl group are formed (Figure 2). The terminal hydroxyl group is left on the zirconium site, while the proton binds to a neighboring oxygen atom. The adsorption energies for a single water molecule at (w)- and (s)-sites are −96 and −160 kJ/mol, respectively (Table 1). The differences to the previous study[7] are due to improved DFT calculations. Haase and Sauer employ the PBE[37,38] functional with pseudopotentials (norm conserving [Kr] core of Zr, supersoft Vanderbilt for O, H, and S), while the PW91 functional with a PAW description (small core on Zr:[Ar]3d¹⁰) is used in the present study. In addition, the former calculation considers only the Γ-point. When passing from a Γ-point calculation to a 2k-point calculation, we find a decrease from 112 to 96 kJ/mol for the adsorption energy of water on the weak site. This decrease of the adsorption energies is not accompanied by a qualitative change of the adsorption structure; i.e., both calculations predict chemisorption.

Upon increase of the water coverage, the second water molecule occupies the second strong site (Figure 3), but the system gains only 85.4 kJ/mol. The initial adsorption of a water molecule influences the neighboring Zr sites in such a way that adsorption of the second molecule becomes much less favorable. This is in line with the normal behavior of decreasing adsorption energy with increasing coverage. For the third water molecule only a weak Zr site is available. It has to insert between the rowlike structures of H₂O molecules adsorbed on strong sites. The energy gain is 45.4 kJ/mol only. This water molecule does
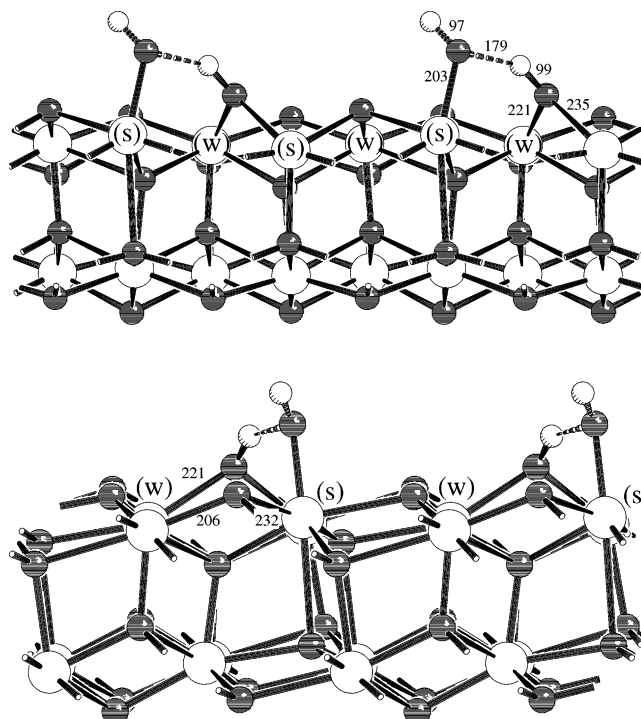

Figure 2. Two different views of the dissociative adsorption of one water molecule with hydrogen bonding [OH⁻,H⁺]. Adsorption on the strong adsorption site Zr(s). For a better overview a 1 × 4 (top) and a 2 × 2 (bottom) surface cell is plotted.

TABLE 1: Cumulative Adsorption Energies of Water Adsorption (kJ/mol) (Read Zr(s) Vertically and Zr(w) Horizontally)

	Zr(w)	pure	H₂O	2H₂O
Zr(s)				
pure		0.	−96.3	−171.6
H₂O	−160.2[a]	−213.0	−178.0	
2H₂O	−245.7[a]	−291.0	−375.6[a]	

[a] This structure appears in the phase diagram of section 3.5.

not dissociate. A fourth water molecule adsorbs on the second weak Zr site completing the monolayer. The energy gain increases again to 84.6 kJ/mol due to hydrogen bonds with water molecules already present (Figure 4).

3.2. SO₃ Adsorption. When two oxygen atoms of an SO₃ molecule are brought into contact with two surface zirconium atoms and the structure is allowed to relax, an additional bond between the sulfur atom and a surface oxygen atom is formed. This surface oxygen atom moves out of the surface and leaves an O²⁻ vacancy near the adsorbed molecule (see Figure 5 for [SO₃]). This kind of tridentate adsorption is characteristic of adsorbed SO₃ in the absence of water. It was found before by Galvan and co-workers[19] for a very simple model of t-ZrO₂, for which no Zr-atom has a bulklike 8-fold oxygen coordination. The adsorption energy for the first SO₃ molecule on two Zr(s) sites is −336.6 kJ/mol (two Zr(w): −258.5 kJ/mol). This is similar to adsorption of water molecules and yields SO₃ rows on the surface (Figure 6). The lateral interactions between two SO₃ molecules due to the periodicity of the model are checked by doubling both lattice vectors a and b, which yields to a slab with a 2 × 4 surface cell. Accordingly, the k-point mesh is reduced to half in every direction. The adsorption energy is −361.1 kJ/mol compared to −336.6 kJ/mol for the 1 × 2 surface cell.

Since SO₃ coordinates to only two surface zirconium atoms, there is space left on the 1 × 2 surface cell for a second SO₃
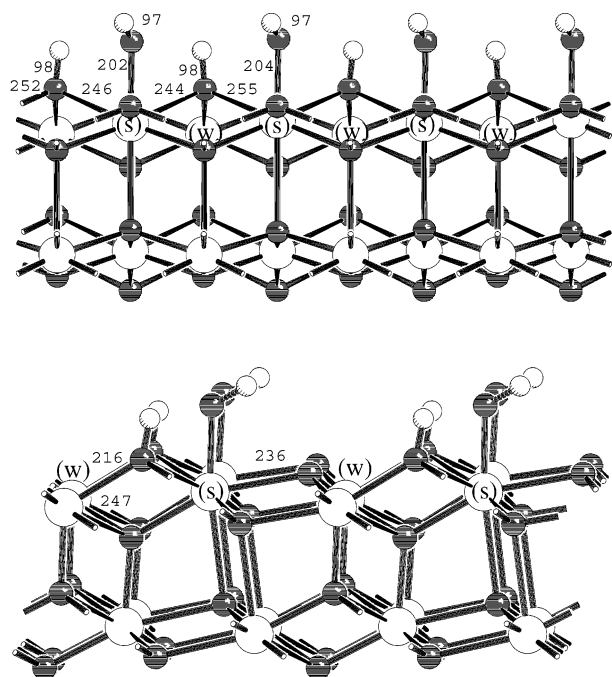
Hydroxylated and Sulfated Zirconia Surfaces

J. Phys. Chem. B, Vol. 108, No. 38, 2004 **14655**

Figure 3. Dissociative adsorption of two water molecules with no hydrogen bonding [2OH$^-$,2H$^+$]. Half monolayer adsorption on the strong adsorption site Zr(s).
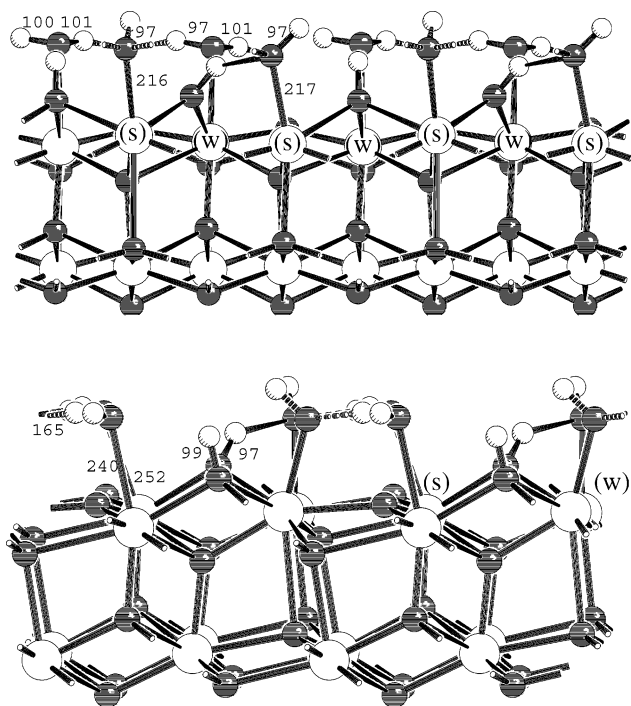

Figure 4. Full monoayer adsorption of water. Dissociative adsorption on the strong site Zr(s); molecular adsorption on the weak site Zr(w) [2OH$^-$,2H$^+$,2H$_2$O]. The bottom part is moved by 0.5a in the paper plane, in comparison with Figure 3.

molecule. Adsorption of the second molecule SO$_3$, which can only coordinate to weak Zr sites, is much less favorable with an adsorption energy of -25.8 kJ/mol (cumulative adsorption energy, -362.4 kJ/mol). Moreover, there are repulsive interactions between the SO$_3$ molecules, indicated by a tilting of about 30° (Figure 7).

3.3. Sulfur Oxide and Water Coadsorption. Coadsorption of SO$_3$ and H$_2$O can be made either with separate SO$_3$ and H$_2$O species or with H$_2$SO$_4$. H$_2$SO$_4$ can dissociate on the surface first in [H$^+$,HSO$_4^-$] and then in [2H$^+$,SO$_4^{2-}$]. The dissociated
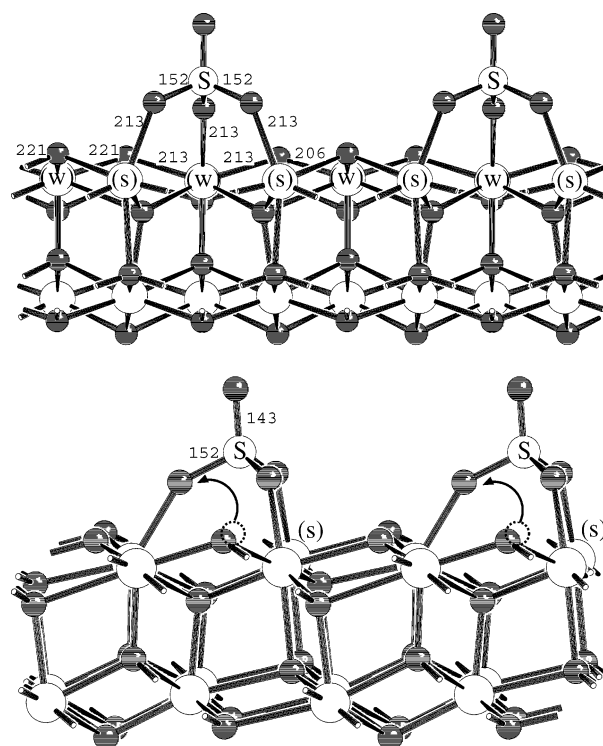

Figure 5. Sulfur trioxide adsorption on two strong Zr(s) sites [SO$_3$]. One oxygen atom of the surface moves up for the third bond to the sulfur atom.
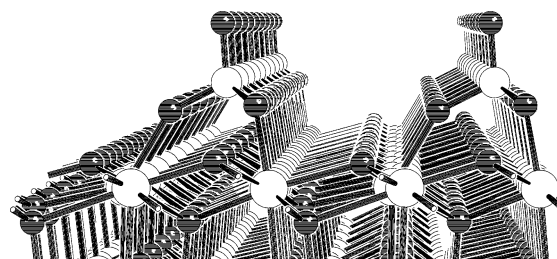

Figure 6. Perspective view of the rowlike superstructure of a single SO$_3$ per unit cell.

protons form bridging hydroxyl groups on the surface. When a SO$_3$ molecule and a H$_2$O molecule are present, SO$_3$ coordinates to the two Zr(s) sites and H$_2$O dissociatively adsorbs at one of the Zr(w) sites. The proton moves to a bridged surface oxygen atom. The SO$_3$ adsorption structure is virtually the same as without water adsorption (Figure 5). The energy gain of 33 kJ/ mol for the coadsorption of water is smaller than the adsorption energy for H$_2$O at a Zr(w) site of the clean surface (-96 kJ/ mol). This indicates a strong influence of SO$_3$ on the next neighboring atoms.

In the gas phase, H$_2$SO$_4$ is more stable by 82 kJ/mol than the separated SO$_3$ and H$_2$O species. On the t-ZrO$_2$(101) surface the most stable isomer of adsorbed H$_2$SO$_4$ is [SO$_3$,H$^+$,OH$^-$]. If we allow heterolytic dissociation of H$_2$SO$_4$ into [H$^+$,HSO$_4^-$] and [2H$^+$,SO$_4^{2-}$], we find stable structures, too. However, the adsorption energies, -292 and -315 kJ/mol, respectively, are smaller than for the [SO$_3$,H$^+$,OH$^-$] adsorbate (-370 kJ/mol).

Addition of the second H$_2$O molecule to the [SO$_3$,H$^+$,OH$^-$] surface structure lowers the energy more (by -50 kJ/mol) than coadsorption of the first H$_2$O. The adsorption energy for the [SO$_3$,H$^+$,OH$^-$,H$_2$O] isomer is -418 kJ/mol (Table 2). This is the largest adsorption energy among all [SO$_3$·2H$_2$O] isomers and due to hydrogen bonding between a terminal hydroxyl group and the S=O oxygen atom (Figure 8).
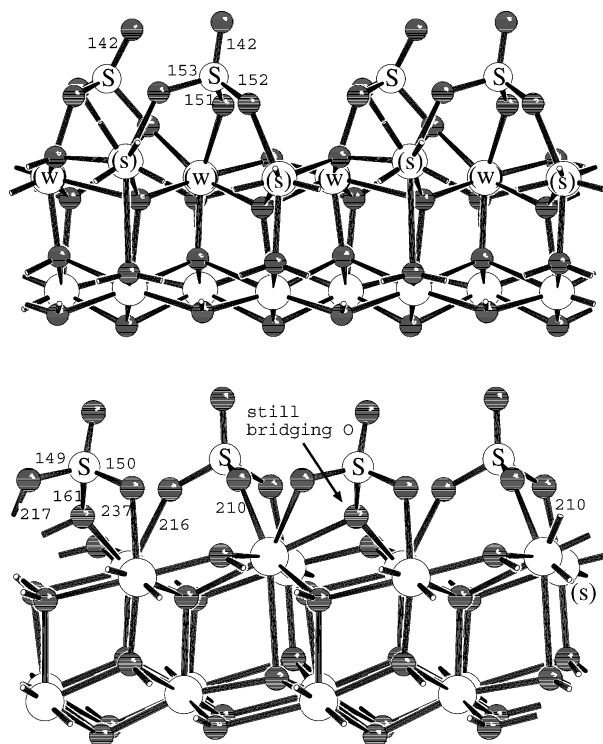
Figure 7. Adsorption of two molecules of sulfur trioxide [2SO$_3$]. All Zr sites are covered. The adsorbates are rotating and tilting to minimize repulsion.

TABLE 2: Cumulative Adsorption Energies of SO$_3$ + mH$_2$O Molecules ($m = 1-4$; kJ/mol; Sulfate Species on the Strong Zr Sites) (Read Zr(s) Vertically and Zr(w) Horizontally)

	Zr(w)	pure	H$_2$O	2H$_2$O	3H$_2$O
Zr(s)					
SO$_3$		-336.6^a	-369.6	-418.0^a	b
HSO$_4^-$,H$^+$		-292.3	-391.6	-365.8	-523.3
SO$_4^{2-}$,2H$^+$		-314.7	-398.7	-367.6	-542.4^a

^{a} This structure appears in the phase diagram of section 3.5. ^{b} Not investigated because the third H$_2$O would open the second adsorption layer.

The trends for coadsorption of water and dissociated acids are less uniform. Energy gains are due to numerous possibilities to form hydrogen bonds. Figure 9 shows this for the adsorption structure [SO$_4^{2-}$,2H$^+$,3H$_2$O]. The most stable structures are therefore the best compromise of adsorbing an acid and stabilizing it by hydrogen bonds.

For a higher concentration of SO$_3$ on the surface (two sulfur atoms per surface unit cell; Table 3), we examine two possible cases: adsorption of two H$_2$SO$_4$ species and adsorption of the H$_2$S$_2$O$_7$ dimer. For the latter case, Figure 10 shows the most stable structure. At the surface, H$_2$S$_2$O$_7$ dissociates into the pyrosulfate anion, S$_2$O$_7^{2-}$, and two protons, which form bridging surface hydroxyl groups. Three oxygen atoms of the pyrosulfate ion coordinate to Zr sites on the surface. Apparently, the fourth possible coordination to a Zr(w) site is too weak to win the competition with the hydrogen bond to a surface OH group. One additional water molecule, which adsorbs molecularly [S$_2$O$_7^{2-}$,2H$^+$,H$_2$O] (Figure 11), creates even more hydrogen-bonding opportunities, but does not change the picture.

The last structure, which appears in the surface phase diagram, is also the most complex one (Figure 12). It includes both a sulfate and a hydrogen sulfate species as well as two water molecules: [SO$_4^{2-}$,HSO$_4^-$,3H$^+$,2H$_2$O]. Three protons have
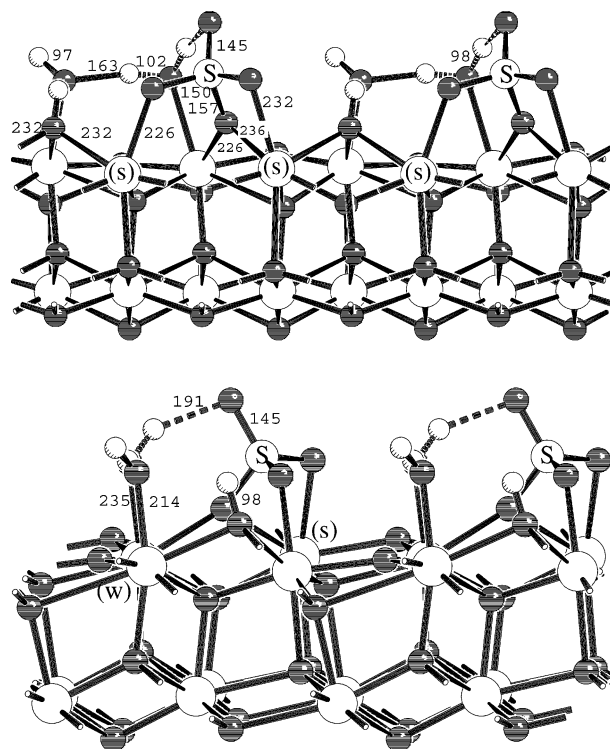
Figure 8. Adsorption of one SO$_3$ molecule together with two water molecules [SO$_3$,OH$^-$,H$^+$,H$_2$O]. All Zr sites are covered.

TABLE 3: Cumulative Adsorption Energies of 2SO$_3$ + mH$_2$O Molecules ($m = 1-4$; kJ/mol; All Sulfate Species Are on the Zr(s) and Zr(w) Sites) (Read Zr(s) Vertically and Zr(w) Horizontally)

	Zr(w)	pure	H$_2$O	2H$_2$O
Zr(s)				
H$_2$SO$_4$,HSO$_4^-$,H$^+$		a	-474.8	a
2HSO$_4^-$,2H$^+$		-517.6	-461.2	a
HSO$_4^-$,SO$_4^{2-}$,3H$^+$		a	a	-589.9^b
2SO$_4^{2-}$,4H$^+$		-456.7	a	a
HS$_2$O$_7^-$,H$^+$		a	-449.7	-490.6
S$_2$O$_7^{2-}$,2H$^+$		-409.1	-533.1^b	-560.2

^{a} For this structure no minimum was found. It converges to another dissociation state. ^{b} This structure appears in the phase diagram of section 3.5.

formed bridging surface hydroxyls. Since there are four surface Zr sites available and two are occupied by H$_2$O, there is monodentate adsorption for the SO$_4^{2-}$ and HSO$_4^-$ species. We end up with a hydrogen-bonded structure with only one free S=O bond, i.e., not involved in any hydrogen bonding.

3.4. Vibrational Frequencies. Table 4 shows the S=O and S–O stretching regions for the surface structures considered (Figure 13).

3.5. Surface Phase Diagrams. Equation 9 defines the Gibbs free energy of formation of a given adsorbate as a function of the chemical potentials of SO$_3$ and H$_2$O or H$_2$SO$_4$ and H$_2$O in the gas phase. The surface phase diagrams (Figures 14 and 15) show the chemical potential region for which a given adsorbate structure has the lowest free energy, i.e. is most stable.

As an upper limit for the chemical potential of the gases, we use $\Delta\mu^{(g)} = 0$. For the lowest chemical potentials we choose values below which no new phases will appear. We select temperatures in the range from room temperature to calcination temperature (1098 K). We do not examine the dependency on H$_2$SO$_4$ partial pressures above 570 K, because in the gas-phase H$_2$SO$_4$ is not stable above about 570 K.
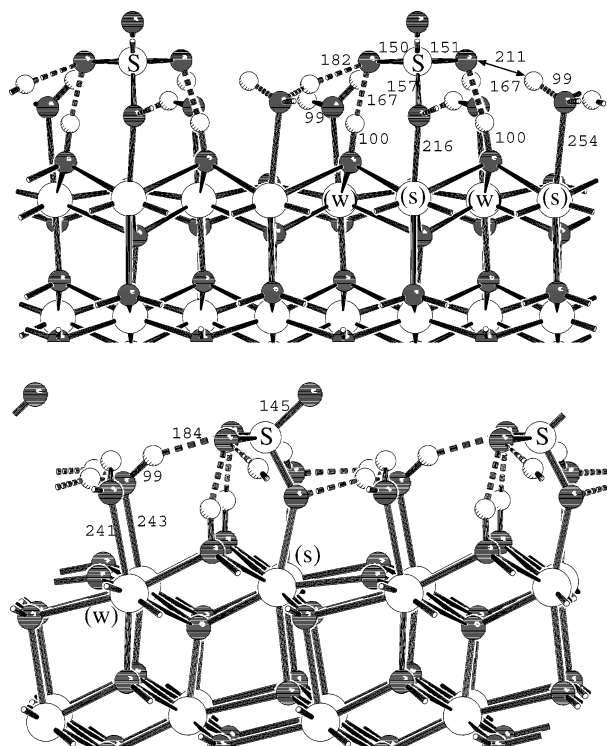
Hydroxylated and Sulfated Zirconia Surfaces

J. Phys. Chem. B, Vol. 108, No. 38, 2004 **14657**

Figure 9. Monodentate adsorption of sulfate on the strong Zr(s) site [SO_4^{2-},2H$^+$,3H$_2$O]. The protons are building bridging hydroxyl groups with surface oxygen atoms. Water molecules are adsorbing on the remaining strong and the two weak Zr sites. They do not dissociate. Strong hydrogen bonding is observed.
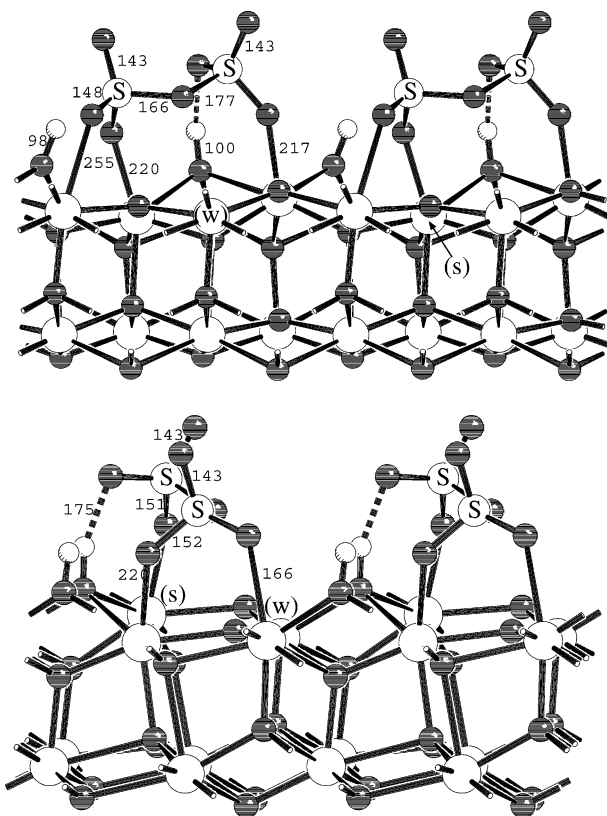
Figure 10. Tridentate adsorption of the pyrosulfate ion on the t-ZrO$_2$-(101) surface [$S_2O_7^{2-}$,2H$^+$]. Two bonds to the strong Zr(s) site; one bond to the weak Zr(w) site. The bottom part is moved by 0.5a in the paper plane, in comparison to Figure 9.
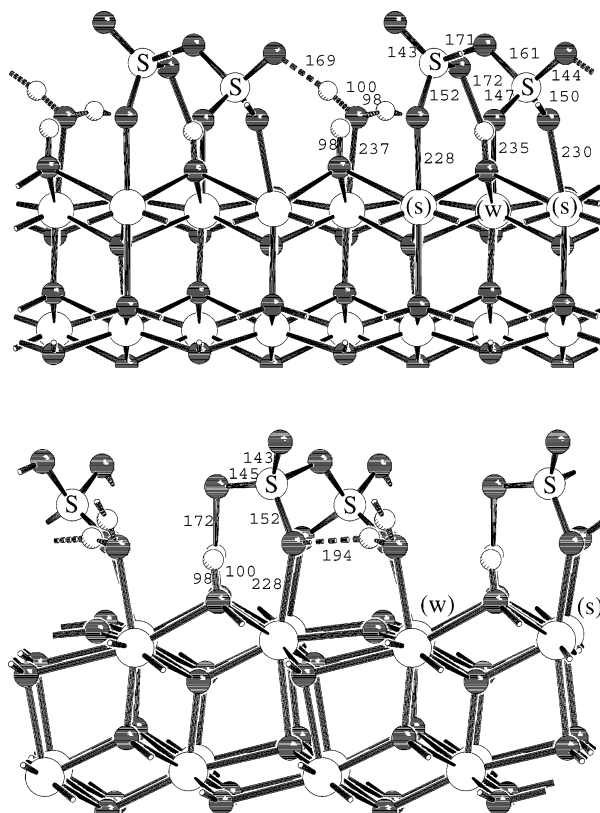
Figure 11. Tridentate adsorption of the pyrosulfate ion on the t-ZrO$_2$-(101) surface accompanied by one water molecule [$S_2O_7^{2-}$,2H$^+$,H$_2$O]. The water molecule provides hydrogen atoms for hydrogen bonding and stabilization of pyrosulfate oxygen atoms.
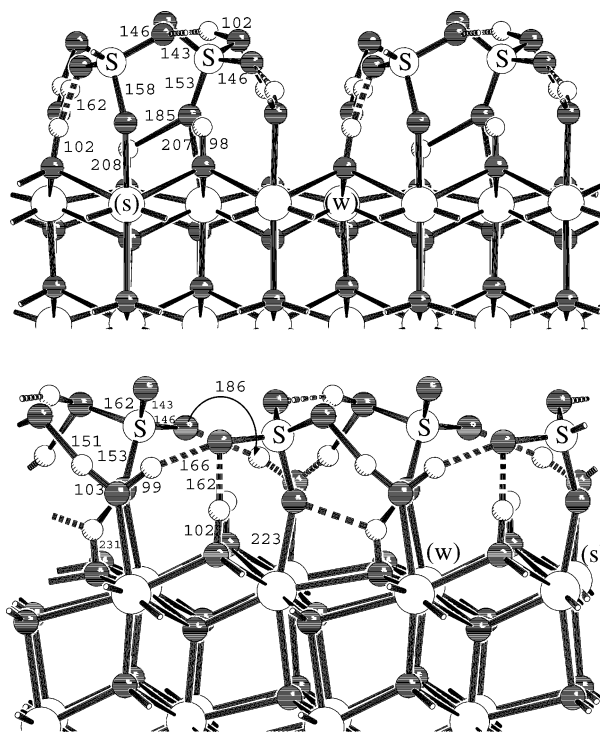
Figure 12. Monodentate adsorption of a sulfate, a hydrogen sulfate, and two water molecules [SO_4^{2-},HSO$_4^-$,3H$^+$,2H$_2$O]. The water molecules set up together through manifold O···H···O and O···H−O interactions a hydrogen-bonded framework.

(right). In the low-H$_2$O−low-SO$_3$ chemical potential corner (low partial pressures) the surface phase diagram predicts no adsorption at all. The entropic part of the Gibbs free energy of the

The diagrams on the top of Figure 14 show the dependency on H$_2$O and SO$_3$ partial pressures for 498 (left) and 898 K

TABLE 4: S=O and S—O Stretch Frequencies (cm^{-1}) for Different Adsorbates^a

	Zr(w)OS=O	Zr(s)OS=O	S—O + δ(Zr—O$_{t/b}$—H)	Zr(w)O—S	Zr(s)O—S
[SO$_3$]		1398		1029	1004, 1001
[SO$_3$,OH$^-$,H$^+$,H$_2$O]		1324		935	1118, 1011
[SO$_4{}^{2-}$,2H$^+$,3H$_2$O]		1310	1143, 1111 / 1077, 1035, 986		935
[HSO$_4{}^-$,SO$_4{}^{2-}$,3H$^+$,2H$_2$O]	1474, 1374 (1187, 1036)^b	1272, 1262, 1195 (1111, 1069, 1057)^b		998	951
[S$_2$O$_7{}^{2-}$,2H$^+$,H$_2$O]	1317	1421, 1214	901, 889	(1174, 1112)^b	(1084, 999)^c
[S$_2$O$_7{}^{2-}$,2H$^+$]	1401^c	1417^d		1131,^{c} 1045	(1199, 992, 969)^d
[2SO$_3$]	(1432, 1406)^e			1120, 1016, 840	1053, 1031, 1005

^{a} Zr(w) and Zr(s) stand for weak and strong Zr sites, respectively. O$_{t/b}$H is a terminal or bridging hydroxyl group, respectively. All frequencies are scaled by 1.073 76. The scale factor is derived from calculations on SO$_3$, H$_2$SO$_4$, and O$_2$S(OCH$_3$)$_2$; see Table S2. ^{b} These modes are due to coupling with Zr/S—O—H angle deformations. ^{c} These modes are due to coupling with Zr(w)OS—O bond stretches. ^{d} These modes are due to coupling with Zr(s)OS—O bond stretches. ^{e} These modes are due to coupling with Zr(w)OS=O stretches Zr(w)OS=O.
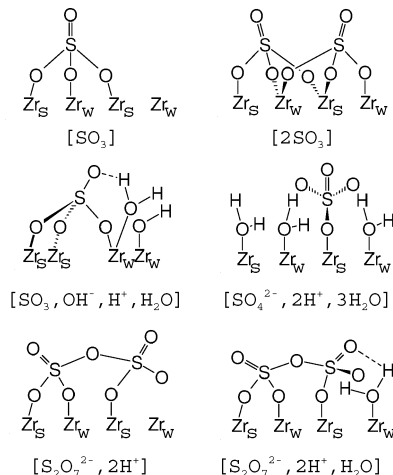

Figure 13. Sulfur-containing surface structures (surface oxygen atoms and bridging hydroxyl groups are not drawn).

gas-phase species is so high that adsorption is not favorable. Moving to higher SO$_3$ chemical potentials (higher SO$_3$ partial pressure), we reach the region of SO$_3$ adsorbed on strong Zr sites (Figure 5) at the value of the chemical potential of SO$_3$ which corresponds to the adsorption energy of SO$_3$. Further increase of the SO$_3$ chemical potential leads to full coverage of the surface with SO$_3$, i.e., adsorption of two SO$_3$ molecules per surface unit cell (Figure 7).

Starting from the low—low corner to higher water chemical potentials, we observe surface hydroxylation, i.e. chemisorption of a single water molecule on the strong Zr site (Figure 2), if the chemical potential of H$_2$O in the gas-phase becomes equal to the adsorption energy. Then, there is a small partial pressure region where chemisorption of two water molecules yields hydroxyl groups on all strong Zr sites (Figure 3). Complete water coverage of the t-ZrO$_2$(101) surface (Figure 4) is reached at even higher partial H$_2$O pressure.

Introducing SO$_3$ at this H$_2$O chemical potential, we reach complex adsorbate structures. At low SO$_3$ chemical potential, we observe a sulfate-adsorbed monodentate on a strong Zr site. It is accompanied by three water molecules that solvate two bridging hydroxyl groups. The latter originates from protons split off the initial sulfuric acid species ([SO$_4{}^{2-}$,2H$^+$,3H$_2$O], Figure 9). At higher SO$_3$ and lower H$_2$O chemical potential, we observe condensation of two sulfate species to a pyrosulfate species ([S$_2$O$_7{}^{2-}$,2H$^+$,H$_2$O], Figure 11). In the high—high corner, two adsorbed sulfate species are found and condensation is no longer favorable ([HSO$_4{}^-$,SO$_4{}^{2-}$,3H$^+$,2H$_2$O], Figure 12). Hence, pyrosulfate will be stable only in a small region of H$_2$O and SO$_3$ partial pressures.

The picture changes if we look at the dependence on H$_2$O and H$_2$SO$_4$ partial pressures (lower part of Figure 14). The pyrosulfate phase ([S$_2$O$_7{}^{2-}$,2H$^+$,H$_2$O], Figure 11) is dominating. Increasing the water chemical potential leads to hydrolysis of [S$_2$O$_7{}^{2-}$,2H$^+$,H$_2$O] to monosulfate ([HSO$_4{}^-$,SO$_4{}^{2-}$,3H$^+$,2H$_2$O], Figure 12). Lowering the H$_2$SO$_4$ chemical potential leads to the previously mentioned phase ([SO$_4{}^{2-}$,2H$^+$,3H$_2$O], Figure 9). In medium chemical potential regions, SO$_3$ accompanied by two water molecules ([SO$_3$,H$^+$,OH$^-$,H$_2$O], Figure 8) is stable. In the high—high corner, there is no qualitative difference from the previously discussed H$_2$O/SO$_3$ phase diagram, because we expect formation of H$_2$SO$_4$ from H$_2$O and SO$_3$ at very high water chemical potentials. At low-H$_2$SO$_4$ chemical potential, we observe the adsorbed water structures as described before for the SO$_3$/H$_2$O plot. We stress that most of the sulfur-containing structures in this study are fully dissociated, except if hydrogen bonding is strong enough to prevent the last dissociation step. This last dissociation step, e.g. from HSO$_4{}^-$ to a SO$_4{}^{2-}$ yields typically about 20 kJ/mol.

Figure 15 shows two phase diagrams which neglect vibrational contributions (eq 8). Qualitatively, they are the same as the phase diagrams in Figure 14, but the absolute partial pressures change. (i.e. a phase transition at 498 K: [2OH$^-$,2H$^+$,2H$_2$O] to [SO$_4{}^{2-}$,2H$^+$,3H$_2$O] (Figure 14 to Figure 15), the SO$_3$ partial pressure changes by about 2 orders of magnitude.) So, we cannot neglect the vibrational contributions to the Gibbs free energy, especially for high temperature if we are going to compare our results with experimentals (Table 5).

The phase diagrams show only the most stable phase for given partial pressures. However, there may be other phases which are only marginally less stable. In Figure 15 the hatched region marks the partial pressure range for which a second phase exists which is not more than 10 kJ/mol less stable than the most stable phase (upper right corners). The difference of 10 kJ/mol corresponds to 1% of the second phase in the equilibrium with the most stable one. The only new structure [S$_2$O$_7{}^{2-}$,2H$^+$,2H$_2$O] differs from the dominating structure [S$_2$O$_7{}^{2-}$,2H$^+$,H$_2$O] by one additional H$_2$O molecule attached to a weak Zr site.

4. Discussion

The results about different surface structures and compositions and their relative stability provide explanations for spectroscopically observed changes of the surface structure of differently prepared SZ during calcination. We start our discussion with the more simple case of a sulfate-free hydroxylated zirconia surface.

Thermogravimetric measurements of water desorption from yttrium-stabilized zirconia powder have been made in the range of 335—1000 K, and the results have been fitted to a two-site
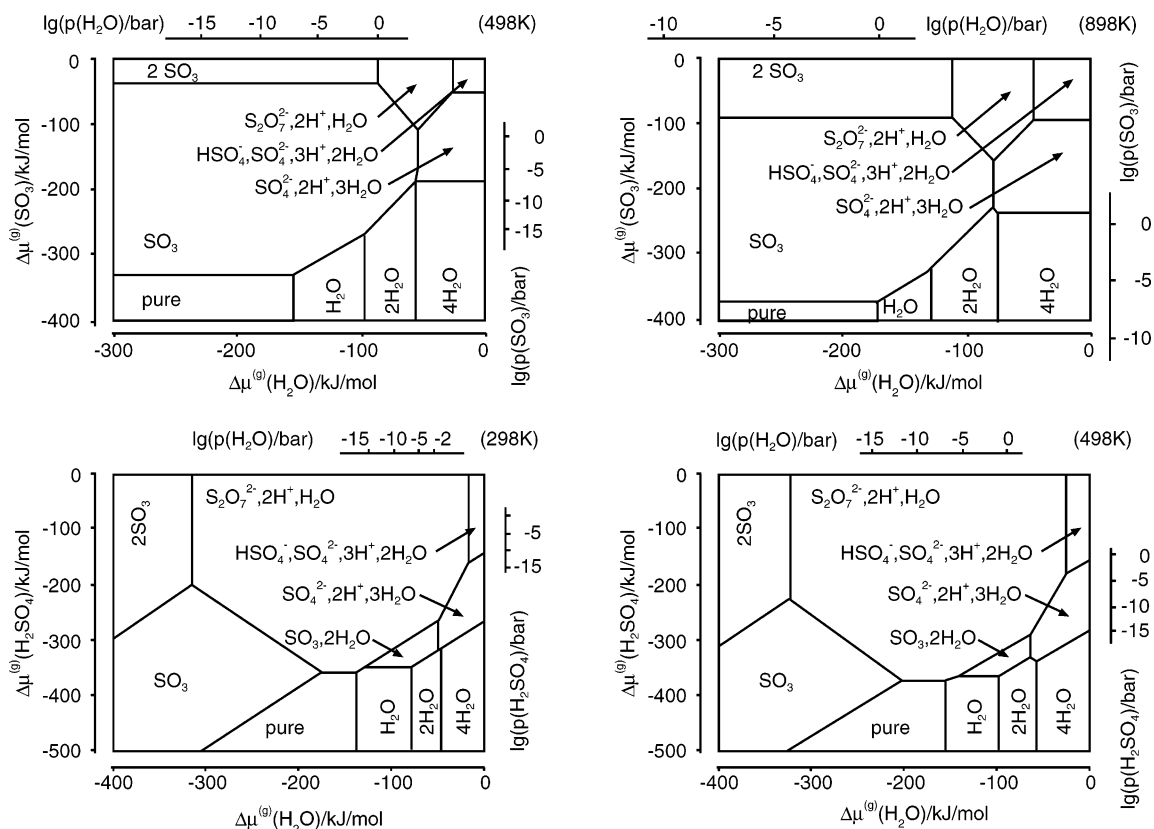
Hydroxylated and Sulfated Zirconia Surfaces

J. Phys. Chem. B, Vol. 108, No. 38, 2004 **14659**

Figure 14. Surface phase diagram for the sulfated t-ZrO_2(101) surface as a function of the chemical potential of SO_3 (top) or H_2SO_4 (bottom) and H_2O. The pressure at two temperatures is drawn in a logarithmic scale. We show the surface phase diagram including vibrational contibutions for the solids after eq 3. [4H_2O] correponds to [2OH^-,2H^+,2H_2O], [2H_2O] to [2OH^-,2H^+], [H_2O] to [OH^-,H^+], and [SO_3,2H_2O] to [SO_3,OH^-,H^+,H_2O].
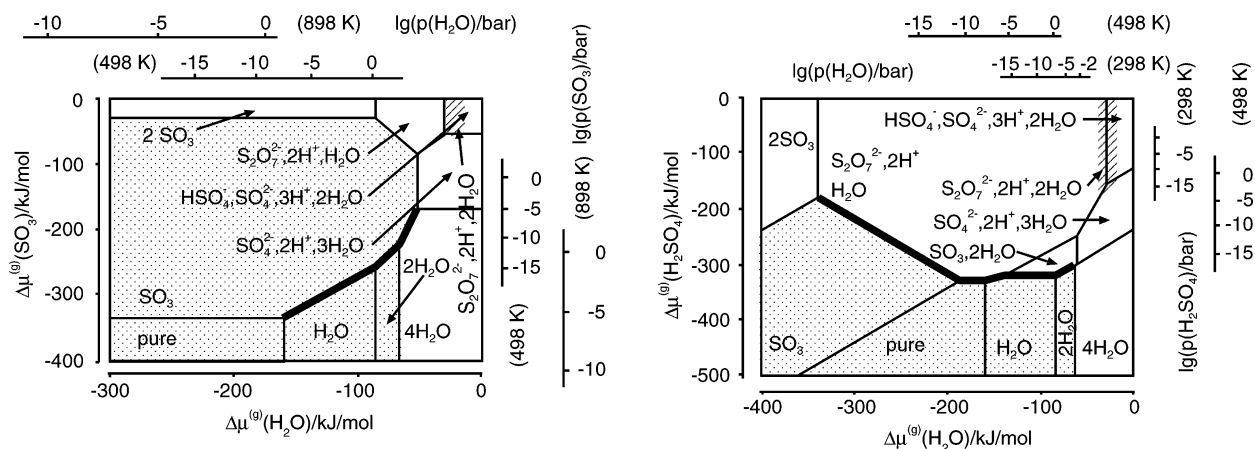
Figure 15. Surface phase diagram for the systems t-ZrO_2(101)/SO_3/H_2O (left) and t-ZrO_2(101)/H_2SO_4/H_2O (right) following eq 8. The hatched region marks the possible existence of a second phase [$S_2O_7^{2-}$,2H^+,2H_2O], which is not more than 10 kJ/mol less stable than the most stable one. The dotted areas mark regions with coordinatively unsaturated Zr site(s).

Langmuir chemisorption model.[40] Enthalpies of adsorption of 94 ± 19 and 70 ± 14 kJ/mol have been derived from this fit. In addition, a BET model has been used for the physisorbed water on top of the chemisorption layer, which results in a heat of adsorption of 47.6 ± 1.4 kJ/mol if the heat of evaporation of liquid water is 40.6 kJ/mol (at 400 K). In this context, chemisorption is understood as dissociative adsorption, leading to surface hydroxyl groups and physisorption as molecular adsorption.

The present results (Figure 16) predict that already below room temperature all molecularly adsorbed water molecules have left the surface and the fully hydroxylated surface, [2OH^-,2H^+], is most stable. Half of the chemisorbed water molecules leave the surface at about 440 K (partial dehydroxy-

lation [2OH^-,2H^+] → [OH^-,H^+] + H_2O) and the last chemisorbed water at about 730 K (complete dehydroxylation). These results support the assumptions made in analyzing the above desorption data. The calculated energies are 56 kJ/mol for molecular desorption (at 298 K), 75 kJ/mol for desorption of the first chemisorbed water (498 K), and 150 kJ/mol for the last step (698 K).

The calculated energies, in particular for the last desorption step, are larger than values derived by fitting the experimental data. However, taking into account the inherent errors of DFT in describing water binding and dissociation energies and the uncertainties in modeling the experiment, the experimental desorption data and the present calculations give a consistent picture of surface hydroxylation and water adsorption on the

TABLE 5: Zero-Point Energy, E_{ZPV}, and Temperature Dependent Contributions to the Gibbs Free Energy, $E(T)$ and $T \times S(T)$, at Various Temperatures and 1 bar Pressure (All Data in kilojoules per mole)

	E_{ZPV}	$E(T)$				$T \times S(T)$			
		298 K	498 K	698 K	898 K	298 K	498 K	698 K	898 K
t-ZrO$_2$(101)	147.7	71.3	168.5	274.9	384.9	128.0	337.2	597.8	893.4
H$_2$O gas phase (vib)	54.5	0.0	0.2	0.8	1.9	0.0	0.3	1.0	2.5
H$_2$O gas phase (rot + trans)		7.4	12.4	17.4	22.4	56.3	102.6	151.6	202.6
SO$_3$ gas phase (vib)	30.3	2.0	7.1	14.1	22.2	2.8	11.1	23.7	39.6
SO$_3$ gas phase (rot + trans)		7.4	12.4	17.4	22.4	74.2	132.5	193.5	256.5
H$_2$SO$_4$ gas phase (vib)	98.4	6.5	19.5	36.2	54.9	9.8	32.8	65.5	105.4
H$_2$SO$_4$ gas phase (rot + trans)		7.4	12.4	17.4	22.4	81.3	144.3	210.1	277.8
gas-phase volume work		2.5	4.1	5.8	7.5				

|	ΔE_{ZPV}	$\Delta E_{vib}(T)$				$T \times \Delta S_{vib}(T)$			
adsorbate		298 K	498 K	698 K	898 K	298 K	498 K	698 K	898 K
[OH$^-$,H$^+$]	11.6	1.5	7.9	15.5	23.5	1.5	12.7	28.6	47.9
[2OH$^-$,2H$^+$]	19.6	5.6	19.5	35.5	51.8	15.6	47.7	89.5	137.7
[2OH$^-$,2H$^+$,2H$_2$O]	50.6	7.2	31.4	60.7	91.6	24.0	78.6	152.2	239.0
[SO$_3$]	14.8	0.0	4.7	10.4	16.5	5.0	18.5	36.7	58.0
[2SO$_3$]	25.8	2.8	12.6	24.2	36.6	21.5	56.8	101.3	151.9
[SO$_4^{2-}$,2H$^+$,3H$_2$O]	62.7	5.2	22.0	42.5	64.1	24.3	70.1	130.1	199.8
[HSO$_4^-$,SO$_4^{2-}$,3H$^+$,2H$_2$O]	70.2	10.6	39.0	73.5	110.1	43.1	120.1	220.4	337.0
[S$_2$O$_7^{2-}$,2H$^+$,H$_2$O]	47.5	7.3	24.5	44.3	65.0	35.1	90.8	160.5	239.4
[SO$_3$,OH$^-$,H$^+$,H$_2$O]	37.5	7.9	30.4	57.0	85.0	38.5	105.2	190.6	288.7
[S$_2$O$_7^{2-}$,2H$^+$]	30.5	9.8	41.6	81.2	124.0	52.1	143.6	263.3	402.9

zirconia surface. What the present calculations add is a detailed picture of the surface structure under varying conditions. This picture is supported by spectroscopic studies. Riemer et al.[41] studied tetragonal ZrO$_2$ by MAS NMR and found two proton resonances at 3.86 and 1.60 ppm. Because the samples were pretreated at 723 K in vacuo and measured under dry N$_2$, the most likely surface structure under these conditions is [OH$^-$,H$^+$] with terminal and bridging hydroxyl groups (Figure 2). The latter give rise to the resonances at 3.86 and 1.60 ppm, respectively. These hydroxyl groups are also seen in IR spectra with bands at 3655−3600 and 3765−3775 cm^{-1}.[42]

An experimental study of SZ covers the temperature region from room temperature up to 773 K.[44] The SZ is made from an amorphous hydrated ZrO$_2$ precursor sulfated with (NH$_4$)$_2$SO$_4$. The calcined material is exposed to 10^{-3} bar water in the apparatus before recording. The first spectra are recorded at 340 K and "vacuum". The spectrum observed under these conditions shows an S=O band at 1250 cm^{-1} (Figure 17a), which becomes sharper and moves to 1360 cm^{-1} if water is removed by pumping and to about 1400 cm^{-1} after heating at 358 K. Increasing the temperature to 773 K yields no further shifts of this band. Figure 16 shows the stability plot for an assumed pressure of 10^{-5} bar.

The only water-rich phase which fits to the observed spectrum in Figure 17 is [SO$_4^{2-}$,2H$^+$,3H$_2$O], because it does not have S=O bands higher than 1310 cm^{-1}. Removing water most likely leads to the [S$_2$O$_7^{2-}$,2H$^+$,H$_2$O] phase (Figure 14, bottom), which—in agreement with the observed spectral changes—has an S=O band around 1421 cm^{-1}.

Infrared spectroscopic measurements of thermolysis of SZ have been made in the range of 873−1173 K at 10^{-6} bar.[43] The sample made of Zr(SO$_4$)$_2$·4H$_2$O is heated for 30 min at 873 K. For the S=O stretching frequency a broad peak with its center at 1398 cm^{-1} is observed (Figure 17b). Increasing the temperature to 1073 K and heating at this temperature for 2 h diminishes the peak and moves it to 1370 cm^{-1} (Figure 17c). Finally the temperature is increased to 1173 K, where all S=O intensity has vanished. These results are explained by the authors with the conversion of pyrosulfate species into monosulfate species.

Figure 16 shows that at the starting temperature (873 K) of this experiment and at a pressure of 10^{-5} bar a pyrosulfate structure accompanied by one water molecule [S$_2$O$_7^{2-}$,2H$^+$,H$_2$O] is indeed the most stable phase. Isobar heating to 1073 K leads to adsorbed [SO$_3$] as the most stable surface phase. The simulated frequencies show the same trend as in the experiment. The [S$_2$O$_7^{2-}$,2H$^+$,H$_2$O] phase shows two S=O modes at 1421 and 1317 cm^{-1}. The last one has only weak intensity in the experiment. The water-free pyrosulfate [S$_2$O$_7^{2-}$,2H$^+$] exhibits
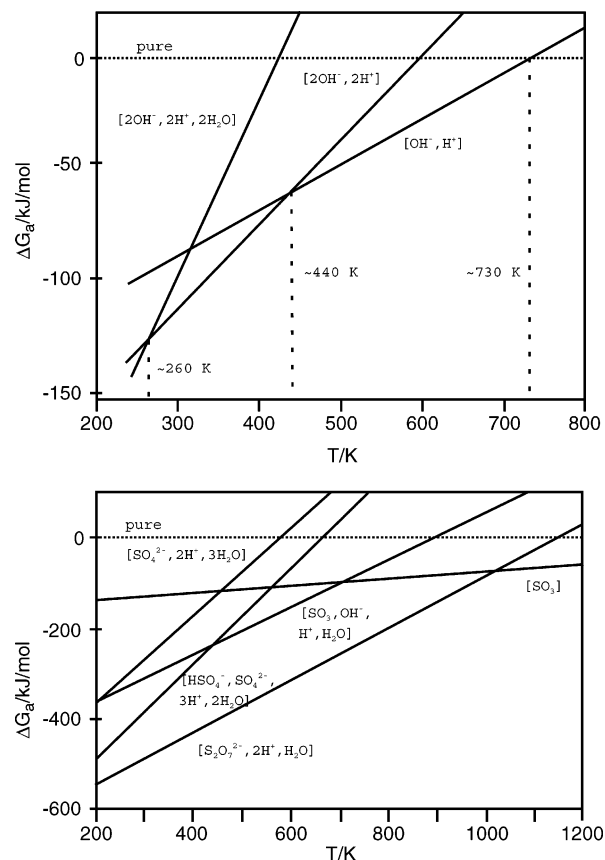
Figure 16. Stability plots for hydrated t-ZrO$_2$(101) at 10^{-2} bar (top) and for sulfated t-ZrO$_2$(101) at 10^{-5} bar (bottom) as a function of T.

Hydroxylated and Sulfated Zirconia Surfaces

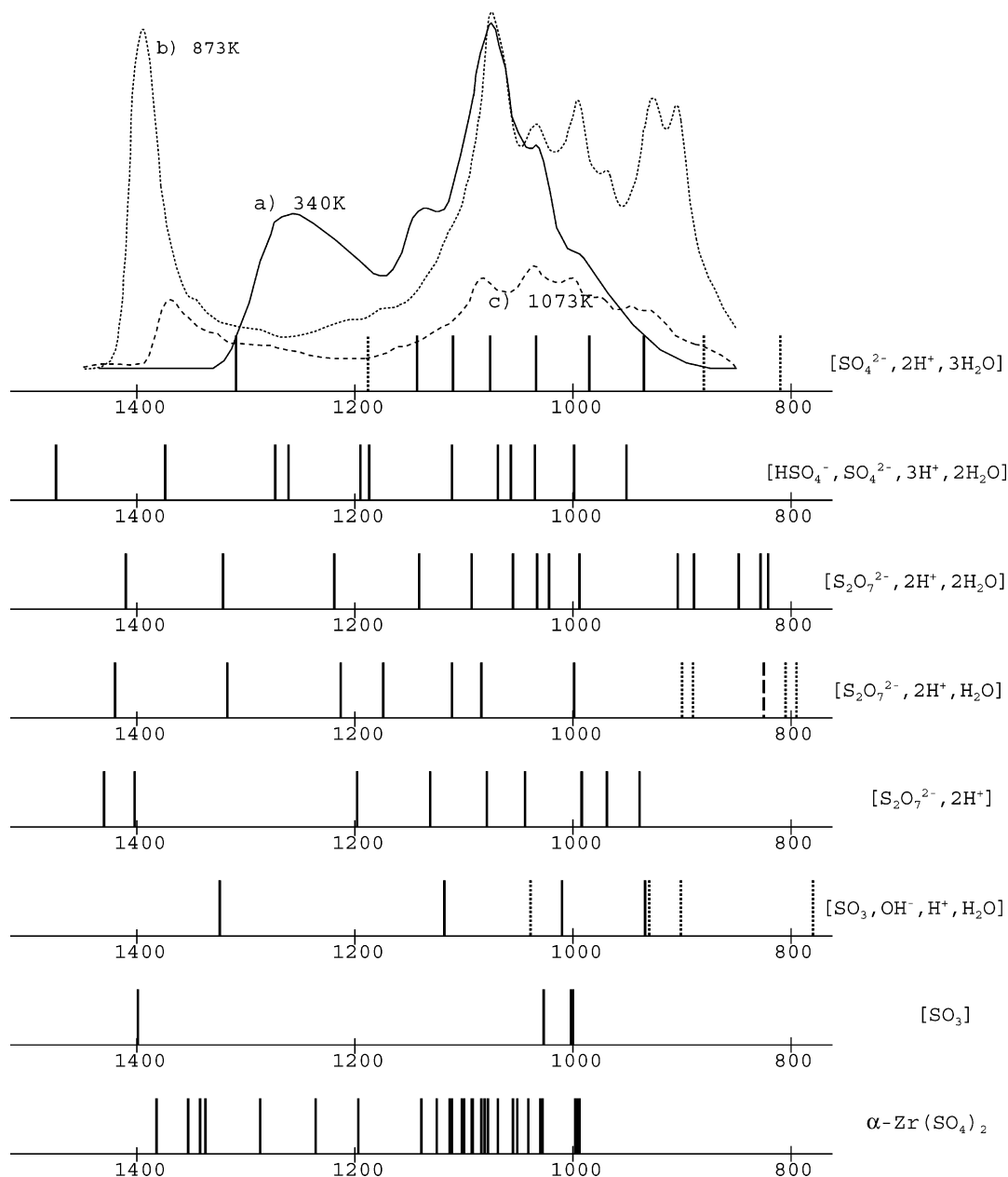*J. Phys. Chem. B, Vol. 108, No. 38, 2004* **14661**

Figure 17. Vibrations in the region of about 1400 cm^{-1} to about 800 cm^{-1}. The experimental spectra are recorded at different temperatures and from different authors (340 K, ref 44; 873 and 1073 K, ref 43). The simulated vibrations for important phases are shown as lines. Dashed lines are pure hydroxl group deformations within the discussed region, where broken lines are surface ZrO_2 vibrations. Additionally, the spectrum of bulk α-$Zr(SO_4)_2$ is shown for reference.

S=O bands at 1417 and 1401 cm^{-1}, and the adsorbed SO_3 molecule, at 1398 cm^{-1}.

The only sulfated phase with Lewis sites is the [SO_3] phase. In the literature, it is claimed that isomerization of *n*-butane takes place only if both Brønsted sites and Lewis sites are present.[12] The dotted areas in Figure 15 mark phases with coordinatively unsaturated Zr sites that may function as Lewis sites. According to the calculated phase diagrams both Lewis and Brønsted sites can be present only at phase boundaries (thick lines in Figure 15), i.e. if two phases coexist.

5. Summary

A broad variety of structures for hydroxylated and sulfated surfaces on t-ZrO_2 have been calculated by DFT with periodic boundary conditions. Their relative stabilities are determined by statistical thermodynamics. We observe a qualitative change of the prevailing sulfate surface species depending on the

sulfatation agent (SO_3 or H_2SO_4). In equilibrium with SO_3 adsorbed SO_3 prevails, whereas in equilibrium with H_2SO_4 a pyrosulfate phase [$S_2O_7^{2-}$,$2H^+$,H_2O] dominates. Higher polymeric sulfates are not observed.

The calculated surface phase diagrams explain infrared spectroscopic findings. Water-rich and sulfate-poor structures do not show S=O bands above 1330 cm^{-1}. Calcination starts with dehydratization, and the simulated sulfate vibrational frequencies are blue-shifted to 1370−1400 cm^{-1}. Frequencies above 1400 cm^{-1} are observed for water-free and two sulfur species per surface unit cell only.

Supporting Information Available: Tables of total energies of selected systems and scaling factors for different SO vibrational modes. This material is available free of charge via the Internet at http://pubs.acs.org.

References and Notes

(1) Holm, V. C. F.; Bailey, G. C. U.S. Pat. 3 032 599, 1962.

(2) Hino, M.; Arata, K. *Chem. Lett.* **1979**, *8*, 477.

(3) Hino, M.; Kobayashi, S.; Arata, K. *J. Am. Chem. Soc.* **1979**, *101*, 6439.

(4) Hino, M.; Arata, K. *Chem. Commun.* **1980**, 851.

(5) Stichert, W.; Schüth, F.; Kuba, S.; Knözinger, H. *J. Catal.* **2001**, *198*, 277.

(6) Benaissa, M.; Santiestaban, J. G.; Diaz, G.; Chang, C. D.; Jose-Yacaman, M. *J. Catal.* **1996**, *161*, 694.

(7) Haase, F.; Sauer, J. *J. Am. Chem. Soc.* **1998**, *120*, 13503.

(8) Ouyang, F.; Kondo, J. N.; Maruya, K.-I.; Domen, K. *J. Chem. Soc., Faraday Trans.* **1996**, *92*, 4491.

(9) Haw, J. F.; Zhang, J.; Shimizu, K.; Venkatraman, T. N.; Luigi, D.-P.; Song, W.; Barich, D. H.; Nicholas, J. B. *J. Am. Chem. Soc.* **2000**, *122*, 12561.

(10) Bolis, V.; Magnacca, G.; Cerrato, G.; Morterra, C. *Top. Catal.* **2002**, *19*, 259.

(11) Zhang, J.; Nicholas, J. B.; Haw, J. F. *Angew. Chem., Int. Ed.* **2000**, *39*, 3302.

(12) Spielbauer, D.; Mekhemer, G. A. H.; Zaki, M. I.; Knözinger, K. *Catal. Lett.* **1996**, *40*, 71.

(13) Babou, F.; Bigot, B.; Sautet, P. *J. Phys. Chem.* **1993**, *97*, 11501.

(14) Babou, F.; Bigot, B.; Coudurier, G.; Sautet, P.; Védrine, J. C. Sulfated Zirconia for *n*-Butane Isomerization. In *Structure and Dynamics of Exchanged Cations in Zeolites as Investigated by Molecular Dynamics and Computer Graphics*; Yates, D., Ed.; Studies in Surface Science and Catalysis, Vol. 90; Elsevier: Amsterdam, London, New York, 1994.

(15) Hong, Z.; Fogash, K. B.; Watwe, R. M.; Kim, B.; Masqueda-Jiménez, B. I.; Natal-Santiago, M. A.; Hill, J. M.; Dumesic, J. A. *J. Catal.* **1998**, *178*, 489.

(16) Hong, Z.; Fogash, K. B.; Dumesic, J. A. *Catal. Today* **1999**, *51*, 269.

(17) Orlando, R.; Pisani, C.; Ruiz, E.; Sautet, P. *Surf. Sci.* **1992**, *275*, 482.

(18) Kanougi, T.; Atoguchi, T.; Yao, S. *J. Mol. Catal. A: Chem.* **2002**, *177*, 289.

(19) Ireta, J.; Aparicio, F.; Viniegra, M.; Galvan, M. *J. Phys. Chem. B* **2003**, *107*, 811.

(20) Hohenberg, P.; Kohn, W. *Phys. Rev.* **1964**, *136*, B864.

(21) Kohn, W.; Sham, L. J. *Phys. Rev.* **1965**, *140*, A1133.

(22) Kresse, G.; Furthmüller, J.; Hafner, J. *Europhys. Lett.* **1995**, *32*, 729.

(23) Kresse, G.; Furthmüller, J. *Comput. Mater. Sci.* **1996**, *6*, 15.

(24) Kresse, G.; Furthmüller, J. *Phys. Rev. B* **1996**, *54*, 11169.

(25) Perdew, J. P. *Phys. Rev. B* **1986**, *33*, 8822.

(26) Perdew, J. P. *Phys. Rev. B* **1986**, *34*, 7406 (erratum).

(27) Perdew, J. P. Unified Theory of Exchange and Correlation Beyond the Local Density Approximation. In *Electronic Structure of Solids 1991*; Ziesche, P., Eschrig, H., Eds.; Akademie Verlag GmbH: Berlin, 1991.

(28) Kresse, G.; Joubert, J. *Phys. Rev. B* **1999**, *59*, 1758. Blöchl, P. E. *Phys. Rev. B* **1994**, *50*, 17953.

(29) Kresse, G.; Joubert, D. *Phys. Rev. B* **1999**, *59*, 1758.

(30) Monkhorst, H. J.; Pack, J. D. *Phys. Rev. B* **1976**, *13*, 5188.

(31) Teufer, G. *Acta Crystallogr.* **1962**, *15*, 1187.

(32) Payne, M. C.; Teter, M. P.; Allan, D. C.; Arias, T.; Joannopoulos, J. D. *Rev. Mod. Phys.* **1992**, *64*, 1045.

(33) Hofmann, A.; Clark, S.; Oppel, M.; Hahndorf, I. *Phys. Chem. Chem. Phys.* **2002**, *4*, 3500.

(34) Frisch, M. J.; Trucks, G. W.; Schlegel, H. B.; Scuseria, G. E.; Robb, M. A.; Cheeseman, J. R.; Zakrzewski, V. G.; J. A. Montgomery, J.; Stratmann, R. E.; Burant, J. C.; Dapprich, S.; Millam, J. M.; Daniels, A. D.; Kudin, K. N.; Strain, M. C.; Farkas, O.; Tomasi, J.; Barone, V.; Cossi, M.; Cammi, R.; Mennucci, B.; Pomelli, C.; Adamo, C.; Clifford, S.; Ochterski, J.; Petersson, G. A.; Ayala, P. Y.; Cui, Q.; Morokuma, K.; Rega, N.; Salvador, P.; Dannenberg, J. J.; Malick, D. K.; Rabuck, A. D.; Raghavachari, K.; Foresman, J. B.; Cioslowski, J.; Ortiz, J. V.; Baboul, A. G.; Stefanov, B. B.; Liu, G.; Liashenko, A.; Piskorz, P.; Komaromi, I.; Gomperts, R.; Martin, R. L.; Fox, D. J.; Keith, T.; Al-Laham, M. A.; Peng, C. Y.; Nanayakkara, A.; Challacombe, M.; Gill, P. M. W.; Johnson, B.; Chen, W.; Wong, M. W.; Andres, J. L.; Gonzalez, C.; Head-Gordon, M.; Replogle, E. S.; Pople, J. A. *Gaussian 98*, Revision A.11.3; Gaussian, Inc.: Pittsburgh, PA, 2002.

(35) Woon, D. E.; Dunning, T. H. *J. Chem. Phys.* **1995**, *103*, 4572.

(36) Reuter, K.; Scheffler, M. *Phys. Rev. B* **2001**, *65*, 035406.

(37) Perdew, J. P.; Burke, K.; Ernzerhof, M. *Phys. Rev. Lett.* **1996**, *77*, 3865.

(38) Perdew, J. P.; Burke, K.; Ernzerhof, M. *Phys. Rev. Lett.* **1997**, *78*, 1396.

(39) Lide, D. R., Ed. *Handbook of Chemistry and Physics*, 74th ed.; CRC Press: Boca Raton, FL, 1994.

(40) Raz, S.; Sasaki, K.; Maier, J.; Riess, I. *Solid State Ionics* **2001**, *143*, 181.

(41) Riemer, T.; Spielbauer, D.; Hunger, M.; Mekhemer, H. A. H.; Knözinger, H. *J. Chem. Soc., Chem. Commun.* **1994**, 1181.

(42) Kustov, L. M.; Kazansky, V. B.; Figueras, F.; Tichit, D. *J. Catal.* **1994**, *150*, 143.

(43) Platero, E. E.; Mentruit, M. P.; Areán, C. O.; Zecchina, A. *J. Catal.* **1996**, *162*, 268.

(44) Morterra, C.; Cerrato, G.; Pinna, F.; Signoretto, M. *J. Phys. Chem.* **1994**, *98*, 12373.

(45) *NIST Standard Reference Data*, http://webbook.nist.gov.

(46) Hintze, P. E.; Kjaergaard, H. G.; Vaida, V.; Burkholder J. B. *J. Phys. Chem. A* **2003**, *107*, 1112.